
Quantification of defects in CFRP plates using active Lock-In thermography and artificial neural networks

Dominik Wolfschläger¹, Konstantin Kromberg¹, Martin Peterek¹, Robert H. Schmitt¹

¹Laboratory for Machine Tools and Production Engineering WZL of RWTH Aachen University, Germany

D.Wolfschlaeger@wzl.rwth-aachen.de

Abstract

Carbon fibre reinforced plastics (CFRPs) are important materials in lightweight constructions as they offer remarkable mechanical properties at a fraction of the mass of conventional materials. The integrity of CFRP structures is crucial for these mechanical properties and must be ensured after potentially harmful impacts. Current research focuses on the detection and characterization of related defects to determine their severity and propose repair concepts for damaged CFRP parts.

In previous studies, physical one-dimensional temperature wave field models have been developed that allow for the measurement of the depth of damages in CFRP parts using phase image series acquired using optical lock-In thermography. These models do not capture the lateral heat flow in thermally excited parts and, hence, pose a major contribution to the measurement uncertainty.

Herein, a novel approach using artificial neural networks (ANNs) for estimating size and depth of defects is presented. ANNs are tools that are able to learn the stochastic behaviour of the heat flow and are expected to provide an improved model compared to the state-of-the-art. To examine this approach, CFRP plates with deterministic known defects are measured using computed tomography (CT) to obtain a reference 3D model. Training data is labelled by mapping the depths and contours of the 3D model onto a sequence of phase images obtained from thermograms captured by an optical lock-In thermography system. Several ANN architectures, including feed-forward (FFNNs) and convolutional neural networks (CNNs), are trained with the labelled data. Reproducibility analysis is performed with similar plates possessing different thicknesses or fibre orientations. Finally, the results obtained with the novel approach are compared to the state-of-the-art.

CFRP, Quality assurance, Machine Learning, Composite Materials, Thermography, Deep Learning, Neural Networks

1. Introduction

Carbon fibre reinforced plastics (CFRPs) provide advantageous mechanical properties and possess only a fraction of the mass of conventional materials. Therefore, there is a large industrial interest in using CFRP, among others in the aerospace and automotive sectors. The structural integrity of the parts is a crucial factor for its mechanical properties [1], subsequently tools are required for enabling an efficient characterization of potential defects [2].

Optical Lock-in Thermography (OLT) is a non-destructive testing (NDT) technique based on the detection of infrared radiation induced by sinusoidally-shaped thermal excitation [3]. The heat flows through the inspected material and is reflected at any inhomogeneity or at the backside of the sample. The reflected waves interfere with the incident waves and the resulting temperature distribution can be monitored by an infrared (IR) camera. The penetration depth of the thermal waves depends on the thermal diffusivity and the excitation frequency, thus, tomographic measurements can be performed by repeated measurements with different excitation frequencies. The lower the frequency, the deeper the thermal wave penetrates into the component [4]. The information of the depth is encoded in the phase difference between the incident and reflected wave. Consequently, OLT is able to determine both the area and the depth of potential defects in CFRP parts. In addition, being an image based measurement technique, it allows for the inspection of large areas and is therefore an economically efficient NDT method.

However, the extraction and characterization of defects utilizing OLT is still a challenging and experience requiring task, because lateral heat flows reduce the contrast between defective and non-defective areas posing a major contribution on the uncertainty of the defect depth estimation.

Classical approaches use physical one-dimensional heat wave field models to simulate the expected phase values for given thermal diffusivities, reflection coefficients, excitation frequencies and defect depths. Comparing with the measured phase value the defect depth can be estimated [5–8]. Thereby, the examined parts must be measured for various excitation frequencies to achieve reasonable depth and size resolution. This significantly increases the time for such measurements. Therefore, methods must be found for reducing the number of necessary measurement cycles and, subsequently, decreasing the inspection time. Moreover, such methods require the measurement of the above mentioned parameters which requires calibrated regions on the investigated parts, a necessity that is usually only available under laboratory conditions.

In literature, several attempts using machine learning techniques for defect detection in CFRP materials have been investigated. Dudzik developed a regressive neural network that predicts the depth of defects in acrylic glass specimens using feature vectors constructed from temperature sequences from different heating stages in active thermography [9]. Duan *et al.* showed that feed-forward neural networks are able to classify which material was left in pores in CFRP materials using thermograms preprocessed with a principal component analysis (PCA) tool [10].

Deep learning models are able to capture complex physical relationships, therefore they offer promising architectures to improve and simplify the process of defect characterization in CFRP components. In order to learn the complex thermal response, take into account and not overestimate the impact of lateral heat flows, following different neural network architectures are investigated on this task. In a first step, this study examines the capabilities of neural networks models for the determination of defect depth in CFRP borehole plates.

2. Experimental setup and data preparation

This section shortly outlines the inspected CFRP samples, the data acquisition of the phase and computed tomography (CT) images. Furthermore, the data labelling process and arrangement are described.

2.1. Carbon fibre reinforced plastic specimen

A set of 17 plates as sketched in figure 1 with dimensions of 150 mm x 150 mm and varying thicknesses composed of Huntsman bisphenol-An epoxy reinforced with TOHO Tenax carbon fibre woven were used for this study.

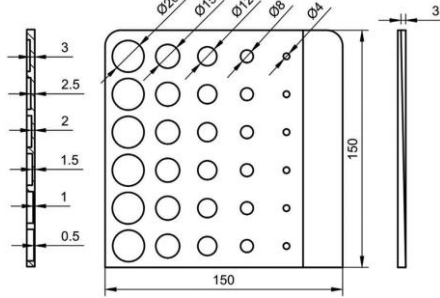


Figure 1. Drawing of a representative CFRP borehole plate specimen as used in this study. Dimensions are in stated in millimetres.

The plates with different wall thicknesses varying from 4.88 mm to 6.09 mm wall thickness and different fibre orientations were used as given in table 1. Boreholes with diameters ranging from 4 mm to 20 mm were incorporated from the back of the plates leaving remaining wall thickness of 0.5 mm, 1 mm, 1.5 mm, 2 mm, 2.5 mm and 3 mm, for each diameter, respectively. Additionally, a wedge with increasing thickness in the range of 0 – 3 mm was milled into the plates to make a continuous wall thickness spectrum in the range of the boreholes depth available. Comparing the resulting depths and areas of the developed models with the deterministic geometries of the incorporated defects, the performance of a given model can be evaluated.

Table 1. Fibre orientation of CFRP borehole plates and the number of associated specimens.

Fibre orientation	# of specimens
[0°/0°/0°/0°/0°/0°/0°/0°]	8
[0°/90°/0°/90°/0°/90°/0°/90°]	5
[+45°/-45°/90°/0°/0°/90°/-45°/+45°]	4

2.2. Phase image data acquisition

Phase images were acquired using an *edevs OTvis 5000* system composed of a *Flir SC5650* cooled infrared camera, two 1000 W halogen lamps, a signal generator and *DisplayImg 6* software. Phase images were acquired for 21 excitation frequencies with the camera settings and measurement parameters provided in table 2. The 21 phase images (cf. Figure 2 (left)) per specimen were exported to 8-bit grayscale images.

2.3. Computed tomography 3D models and image labelling

The CFRP plates are scanned using a *Werth TomoScope HV Compact Computer Tomograph* to obtain a three-dimensional model providing the ground truth wall thicknesses for labelling the phase images for training the neural networks.

Given the volume of the plates a minimal voxel size of 100 x 100 x 100 μm^3 is achieved. A wall thickness analysis is performed using the software *VGSTUDIO MAX 2.2*. Herein, the coordinate system of the 3D image acquired by the CT is oriented such that the x- and y-axes correspond to the x and y directions of the thermography phase images. The z-axis is chosen for the wall thickness determination, where the frontside of the plates is located at z=0 mm. The results of this step is a two-dimensional tensor containing the true depth information for each pixel with voxel resolution.

Table 2. Setting parameters during image acquisition of the OLT system.

Parameter	Value
Image size	512 px x 512 px
Integration time	2000 μs
Frame rate	100 Hz
Focal length	3001 mm
Excitation frequencies	[0.5, 0.4, 0.3, 0.2, 0.15, 0.125, 0.1, 0.09, 0.08, 0.07, 0.06, 0.05, 0.045, 0.04, 0.035, 0.03, 0.0275, 0.025, 0.0225, 0.02, 0.005] Hz
Cycles	3 conditioning and 3 measurement cycles

In order to fuse the phase image and wall thickness data, both the CT matrix image and the phase images must be segmented and scaled such, that the pixels are aligned with each other. The segmentation is performed manually with an interactive segmentation software tool, because this procedure proved to be more robust compared to automated segmentation algorithms based on gray value thresholds or edge detection algorithms. The result of this step is a binary mask for CT and thermography images. Since the height and width of a pixel in a phase images is approximately 0.3 mm and, thus, larger than the voxel size, the voxels must be subsampled to match the size of the thermal image data.

Figure 2 (right) shows the result of the thickness determination. Thicknesses around 7 mm at the upper edge of the plate originate from epoxy remnants from the manufacturing process.

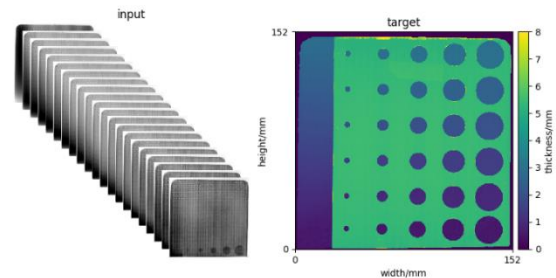


Figure 2. Stacked input data of thermography phase images for 21 excitation frequencies (left), that are labelled with the wall thickness information retrieved from a CT measurement (right).

2.4. Data format

The input data is arranged as $\mathbf{X} \in \mathbb{R}_{N \times H \times W \times C}$ and the output data is of the shape $\mathbf{Y} \in \mathbb{R}_{N \times H \times W}$, where N corresponds to the total number of CFRP samples ($N=17$), H and W are the height respectively the width of the images ($H=W=512$ px) and C is the number of channels, which is equal to the number of excitation frequencies ($C=21$). The data is split into training, validation and test sets to perform the training and evaluate the performance

of the ANN. The fibre orientation has a significant influence on the physical properties [7], therefore all different types are represented in each of the three sets. The number of specimens in the test set is four, three in the validation set and the remaining are used for training.

3. Model Architectures

This section summarizes the examined NN architectures discusses commonly used parameter settings. Furthermore, the investigated model topologies are reported.

3.1. Data exploration

Training can be executed image-wise or pixel-wise. In the case of pixel-wise training, the NN must map the sequence of phase values represented by a sequence of gray values onto thickness. As shown in Figure 3 discrimination of the thicknesses can be found based on such sequences.

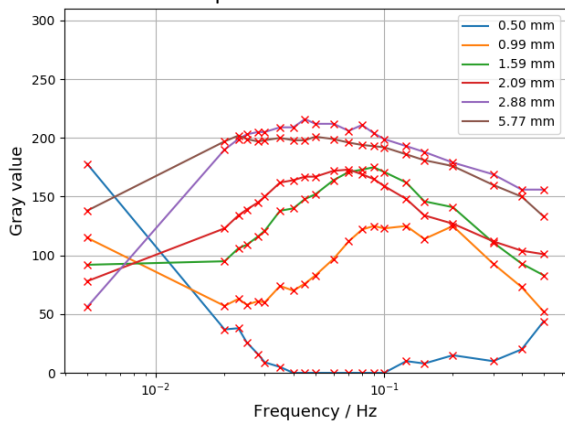


Figure 3. Measured gray values for different excitation frequencies at CFRP plate locations with different nominal thicknesses. It can be observed that both shape and normalization differ for different thicknesses. Subsequently, a discrimination of different thicknesses based on a sequence of gray values can be found.

3.2. Model configurations and parameters

Opposed to the above mentioned traditional approaches where the relationship between phase shift and corresponding thickness of a given material is estimated by a physical model and stored in a lookup table, herein the interdependence is modeled using ANNs. Feed-forward neural networks (FFNNs) are able to recognize simple patterns and are used to determine a continuous function which maps a series of phase shift values onto a thickness. In the following sections, FFNN models are trained pixel-wise and image-wise, whereby, for the latter case the input images are flattened, which results in a smaller number of training samples per epoch [11]. The activation function of proceeding hidden layers is alternating between *tanh* and *ReLU*. Long short-term memory neural networks (LSTMs) have the ability to take temporal dependencies into account and do not expose the vanishing- or exploding gradients problem [12]. LSTM models are trained pixel-wise such that the phase shifts at a fixed position in the image are fed to the model as a time sequence. *Tanh* is applied on the forward output and sigmoid functions are used on the recurrent output of the hidden layers. Convolutional neural networks (CNNs) are able to learn features from images [13] and are the most common approach to solve computer vision problems as e.g. image classification, object recognition and depth estimation [14,15,16]. Last-mentioned models are applied to estimate the wall thicknesses. Since thickness is a positive and real-valued number, the output layer of all studied models is always a fully

connected dense layer with *ReLU* activation function. As training criterion is the mean absolute error (MAE) as stated in equation 1 is chosen. Furthermore, the number of units of the output layer is either 1 for pixel-wise training or 262 144 (512 x 512) for image-wise training.

$$MAE = \frac{1}{N} \sum_{n=0}^{N-1} |y_n - x_n| \quad (1)$$

To ensure convergence weights are initialized using Glorot initialization [17] by drawing samples from a uniform distribution within an interval which depends on the number of inputs and outputs of each layer. Biases are always initialized with zeros and the recurrent weight matrices are orthogonal with random values from a normal distribution. Moreover, early stopping is incorporated to avoid overfitting. Additionally, a random permutation of the pixels is applied in the case of pixel-wise training. Nadam optimizer and a batch size of 64 are used to update the learning parameters. In order to increase performance and generalization of the models and speed up convergence, common data normalization techniques are investigated. Models are trained without normalization (raw pixel values), with zero-one scaling (division by 255), zero-mean (subtract by the mean) and zero-mean/unit-variance (subtraction by the mean and division by the square root of the variance). The examined number of hidden layers for each model varies between 2, 4 and 8 while the number of units for the FFNNs and LSTMs is 16, 32, 64, 128 or 256. For the 2D convolutional case filters of size 4, 8, 16, 32, 64 or 256 with a kernel size of 3 are used and a subsequent maximum pooling with a window size of 4x4 after each layer is applied.

4. Experimental results

Table 3 shows the best two models for each network category and normalization method combination. Performance is evaluated using the MAE. One can observe that image-wise training for CNNs and FFNNs results in the worst performance. Due to the fact that the whole image information is passed through these models at once, they tend to learn a fixed shape representation of the investigated specimen as depicted in figure 1 but the overall estimation of the wall thickness is poor. Normalizing the input for FFNNs does not show significant effect because the average thickness deviation for pixel-wise training is in the range of 0.7 mm – 0.84 mm. Whereas for LSTMs zero-one scaling is not favourable. Zero-mean and zero-mean/unit-variance tend to be a slightly better normalization for CNNs.

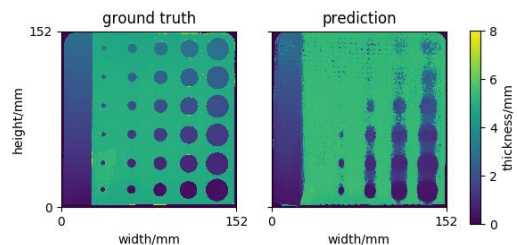


Figure 4. Ground truth and prediction of LSTM 2x64.

Generally it can be said that smaller models with a few layers and less than 256 units for each layer can outperform larger ones on this task. Figure 4 shows the ground truth on the left and the corresponding prediction of the LSTM model with two hidden layers and 64 units per layer on the right. It can be seen that the predicted wall thickness and the thickness of the wedge generally are overall well modeled. Small boreholes with a diameter of up to 8 mm can be detected as well, but the lateral heat flow between nearby defects is not well separated.

Table 3. Comparison of different models and normalization techniques. Best models according to MAE are highlighted in bold..
*filter size for the convolutional case **image-wise training for FFNNs.

Model	Normalization Method	#		MAE	
		layers	units*	train	test
FFNN	none	2	256	0.6	0.78
		4	256	0.73	0.82
	zero-one scaling	2	16	0.5	0.7
		8	32	1.63	1.6**
	zero-mean	2	32	0.57	0.8
8		32	1.8	1.77**	
zero-mean/unit-variance	4	64	0.47	0.71	
	4	256	0.43	0.74	
LSTM	none	2	64	0.47	0.7
		4	16	0.43	0.76
	zero-one scaling	4	128	0.21	0.95
		8	128	1.6	1.76
	zero-mean	2	128	0.5	0.76
2		32	0.36	0.79	
zero-mean/unit-variance	8	32	0.7	0.83	
	2	128	0.23	0.86	
CNN	none	4	64	2.1	1.55
		4	256	2.54	1.78
	zero-one/ scaling	4	16	1.86	1.81
		4	64	2.35	1.89
	zero-mean	4	64	1.27	1.31
4		32	1.37	1.32	
zero-mean/unit-variance	4	16	1.35	1.29	
	4	64	1.49	1.31	

Moreover, the model captures features of the fibre orientation which cause small variations of the predicted thickness.

Figure 5 shows the relative deviation between ground truth depth and predicted depth for each of the specimen from Figure 4. Deviations for each bore hole are computed using the median of a circle with a radius of seven pixels as proposed in [7]. The results show that except for small boreholes of 4 mm diameter and large wall thicknesses of more than 2 mm an overall good prediction is achieved. The results cannot outperform the minimal deviation of state-of-the-art methods (<10% at diameters 8 mm and depth of 2.5 mm) [7], but show smaller deviations for a large number of boreholes than Spießberger [6] and do not require the measurement of material parameters such as the thermal diffusivity. The inclusion of measurement uncertainty in ANN is still an objective of current research in computer sciences and mathematics [18]. Therefore, this study does not include an assessment of the measurement uncertainty. Instead, the trained model was applied on other plates inspected under the same measurement conditions showing comparable results. In order to make the model robust against changing measurement conditions, retraining is required using an extended data set that incorporates varying conditions.

5. Conclusion

This study showed that ANN are able to provide an accurate estimation of the depth of defects in CFRP parts. Although, the accuracy of state-of-the-art approaches is not reached for the full range of defect depth and diameters, the authors' approach show that similar results are achievable with less overhead of the measurement method.

Compared to other approaches using Machine Learning techniques, the proposed models already provide small deviations even without an extensive preprocessing or feature extraction, making it exceptionally simple. It was pointed out that image-wise training in the case of CNN and FFNN models unveils worse performance, whereas pixel-wise training using small LSTM and FFNN topologies yields meaningful results.

6. Future work

Planned studies aim at investigating the ability of the proposed model to estimate the lateral size of defects. Similarly, no hyperparameter optimization has been performed yet. In order to reduce the number of measurement cycles, the impact on the accuracy of the prediction, when training is performed with less than 21 channels, must be investigated. Finally, the application of the model on impact damaged CFRP plates rather than artificial specimens must be performed.

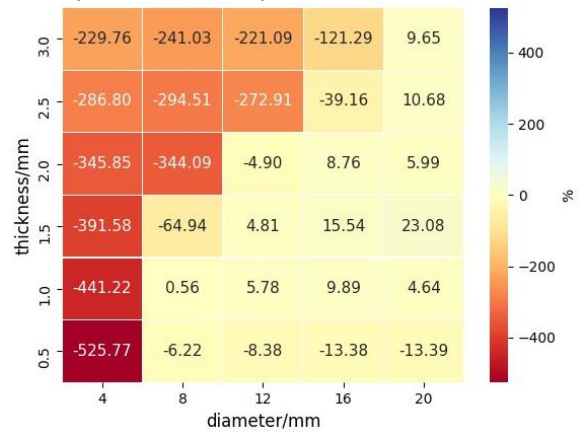


Figure 5. Depth deviation for LSTM 2x 64. Negative values imply under estimation, positive values mean over estimation of the true thickness.

Acknowledgements

This work is supported by the Deutsche Forschungsgemeinschaft DFG within the scope of the German-Brazilian Research Initiative BRAGECRIM (reference SCHM1856/59-1).

References

- [1] Dillenz A, Zweschper T, Spießberger C 2011 *Lightweight Design* vol 5 pp 12–8
- [2] Losch D, Ekanayake S, Nienheysen P, Bethlehem-Eichler K, Schmitz R, Bier S and Roßmann J 2016 *Int. Symp. on Robotics and Manufacturing Automation* vol 2
- [3] Jüngert A, Große C, Aderhold J, Meinschmidt P, Schlüter F, Förster T, Felsch T, Elkmann N, Krüger M and Lutz O 2009 *ZfP-Zeitung* vol 115 pp 43–9
- [4] Gleiter A 2011 *Mess- und Auswertemethoden für die dynamische Thermografie* Stuttgart
- [5] Zöcke C 2009 *Quantitative analysis of defects in composite material by means of optical lock-in thermography* Metz
- [6] Spießberger C 2012 *Merkmalsanalyse mit thermischen Wellen in der zerstörungsfreien Werkstoff- und Bauteilprüfung* Stuttgart
- [7] Ekanayake S 2019 *Metrological characterization of CFRP-damages using optical lock-in thermography* Aachen
- [8] Ekanayake S, Gurram S and Schmitt RH 2018 *Composites Part B: Engineering* vol 147 pp 128–34
- [9] Dudzik S 2013 *Metrology and Measurement Systems* **20** vol 3 pp 491-500
- [10] Duan Y *et al.* 2019 *NDT & E International* vol 107 pp 1021-47.
- [11] Goodfellow I, Bengio Y and Courville A 2016 *Deep Learning* Cambridge
- [12] Hochreiter S and Schmidhuber J 1997 *Neur. Comp.* **9** vol 8 pp 1735–80
- [13] Indolia S, Goswami A, Mishra SP and Asopa P 2018 *Proc. Computer Science* vol 132 pp 679–88
- [14] Simonyan K and Zisserman A 2014 *e-prints:arXiv:1409.1556*
- [15] Szegegy C, Toshev A and Erhan D 2013 *Proc. Int. Conf. on Neural Information Processing Systems* **26** vol 2 pp 2553–61.
- [16] Fu H, Gong M, Wang C, Batmanghelich K and Tao D 2018 *IEEE/CVF Conf. on Computer Vision and Pattern Recognition* pp 2002-11
- [17] Glorot X and Bengio Y 2010 *Proc. of AISTATS* vol 9 pp 249-56
- [18] Osawa K, Swaroop S, Jain A, Eschenhagen R, Turner R, Yokota R, Khan M E 2019 *Proc. of NeurIPS* pp. 4287-99